

Galaxy And Mass Assembly (GAMA): The group H I mass as a function of halo mass

Ajay Dev,^{1*} Simon P. Driver,¹ Martin Meyer,¹ Sambit Roychowdhury,^{1,2,3}
 Jonghwan Rhee,^{1,2} Adam R. H. Stevens,¹ Claudia del P. Lagos,^{1,2,4}
 Joss Bland-Hawthorn,⁵ Barbara Catinella,^{1,2} A. M. Hopkins,⁶ Jonathan Loveday,⁷
 Danail Obreschkow,^{1,2} Steven Phillipps,⁸ Aaron S. G. Robotham¹

¹International Centre for Radio Astronomy Research, University of Western Australia, M468, 35 Stirling Highway, Perth, WA 6009, Australia.

²ARC Centre of Excellence for All Sky Astrophysics in 3 Dimensions (ASTRO 3D), Australia.

³University Observatory Munich (USM), Scheinerstr. 1, 81679 Muenchen, German.

⁴Cosmic Dawn Center (DAWN), Denmark.

⁵Sydney Institute for Astronomy, School of Physics A28, University of Sydney, NSW 2006, Australia.

⁶Australian Astronomical Optics, Macquarie University, 105 Delhi Rd, North Ryde NSW 2113, Australia.

⁷Astronomy Centre, University of Sussex, Falmer, Brighton, BN1 9QH, UK.

⁸H.H. Wills Physics Laboratory, University of Bristol, Tyndall Avenue, Bristol, BS8 1TL, UK.

ABSTRACT

We determine the atomic hydrogen (H I) to halo mass relation (HIHM) using Arecibo Legacy Fast ALFA survey H I data at the location of optically selected groups from the Galaxy and Mass Assembly (GAMA) survey. We make direct H I detections for 37 GAMA groups. Using H I group spectral stacking of 345 groups, we study the group H I content as function of halo mass across a halo mass range of $10^{11} - 10^{14.7} M_{\odot}$. We also correct our results for Eddington bias. We find that the group H I mass generally rises as a function of halo mass from 1.3% of the halo mass at $10^{11.6} M_{\odot}$ to 0.4% at $10^{13.7} M_{\odot}$ with some indication of flattening towards the high-mass end. Despite the differences in optical survey limits, group catalogues, and halo mass estimation methods, our results are consistent with previous group H I-stacking studies. Our results are also consistent with mock observations from SHARK and IllustrisTNG.

Key words: galaxies: groups: general – galaxies: haloes – radio lines: general

1 INTRODUCTION

The effect of environment on the neutral gas content of galaxies is an important driver of galaxy evolution (Cortese et al. 2021). It has been well established that galaxies in higher density environments, such as large groups and clusters, are deficient in neutral atomic hydrogen, H I, compared to those found in the field (Haynes et al. 1984; Solanes et al. 2001; Kilborn et al. 2009; Chung et al. 2009; Cortese et al. 2011; Brown et al. 2017). A number of potentially important effects drive this trend, such as the gravitational interactions between galaxies (tidal stripping, galaxy harassment; Moore et al. 1996) and the interaction of galaxies with the intra-group or intra-cluster medium (ram-pressure stripping, strangulation; Gunn & Gott 1972; Balogh & Morris 2000). Understanding the balance between these processes, their combined effect, and their evolution with time, remains a core goal for galaxy evolution studies, given

the importance of gas as the fuel for star formation and galactic mass assembly.

A particularly useful global observable to constrain these effects is the scaling, and evolution of the H I content as a function of the halo mass, which is dominated by dark-matter (DM). Models that trace and predict the (multiphase) cool-gas content of galaxies have undergone significant developments in recent years, both in cosmological semi-analytic models (Obreschkow et al. 2009; Lagos et al. 2011; Popping et al. 2014; Lu et al. 2014; Lagos et al. 2018), and hydrodynamical simulations (Lagos et al. 2015; Crain et al. 2017; Davé et al. 2017; Diemer et al. 2018; Stevens et al. 2019). Directly relating H I to halo mass provides a valuable observational end-to-end constraint for these models. In doing so, we link the input DM mass distribution for semi-analytic modelling techniques to the desired simulation output product of H I mass. However, making this observational link presents a number of challenges, including the difficulty of detecting H I beyond the relatively local Universe for evolutionary studies, the increasing low-mass limit to which H I

* E-mail: ajay.dev@research.uwa.edu.au

can be detected as a function of redshift, and the ancillary dataset requirements for estimating host halo masses.

Deeper H I surveys along with improved galaxy group catalogues have resulted in empirical studies of the H I-to-halo mass relation (HIHM) being conducted. [Obuljen et al. \(2019\)](#) constrained the HIHM relation as a power law by studying the abundance and clustering of Sloan Digital Sky Survey (SDSS, [York et al. 2000](#)) optically selected H I sources from Arecibo Legacy Fast ALFA survey (ALFALFA, [Giovanelli et al. 2005](#)). [Li et al. \(2022\)](#) estimated the HIHM relation using the H I mass function constructed using an H I mass estimator calibrated with the Extended Galaxy Evolution Explorer Arecibo Sloan Digital Sky Survey (xGASS, [Catinella et al. 2018](#)) sample. One method that has undergone substantial development in recent years, which has improved the measurement of H I at larger distances and lower masses, is H I spectral stacking.

The spectral stacking technique couples H I survey data with optical redshifts in the same region of sky to enable the co-addition of H I emission from multiple sources, whether or not they are directly detected in the H I image cubes. The power of this method was first demonstrated for H I by [Zwaan \(2000\)](#) and [Chengalur et al. \(2001\)](#). Several studies have since used H I stacking to calculate the H I cosmic density at redshifts higher than those available from blind H I surveys ([Lah et al. 2007](#); [Delhaize et al. 2013](#); [Rhee et al. 2013, 2016, 2018](#); [Bera et al. 2019](#); [Hu et al. 2019](#); [Chowdhury et al. 2020](#); [Hu et al. 2020](#); [Chen et al. 2021](#)). [Brown et al. \(2015\)](#) used stacking of H I data from the ALFALFA survey to examine the relationship between gas fraction and star formation properties of galaxies. ALFALFA has also been used to explore the effect of environment through stacking ([Fabello et al. 2011, 2012](#)) in combination with SDSS data, finding evidence of ram-pressure stripping in high density environments for galaxies with stellar mass less than $10^{10.5} M_{\odot}$. Moving into kinematic studies, [Meyer et al. \(2016\)](#) used H I stacking to recover the Tully-Fisher relation from H I Parkes All Sky Survey data ([Meyer et al. 2004](#)). Recently, [Rhee et al. \(2023\)](#) performed H I stacking of galaxies in different halo mass bins to study the H I content for different color, environmental effects, H I gas fraction scaling relation, H I-stellar mass relation, cosmic H I density as well as the HIHM relation with the Deep Investigation of Neutral Gas Origins (DINGO, [Meyer 2009](#); [Rhee et al. 2023](#)) early science data. [Roychowdhury et al. \(2022\)](#) performed group spectral stacking using ALFALFA and DINGO pilot survey data to study the variations of H I mass to stellar mass fraction as a function of stellar mass and star formation rate.

While clearly having a number of advantages for extending the redshift and mass ranges over which H I can be studied, stacking has some drawbacks. One of the most significant in single-dish data, is the effect of confusion, where the desired H I signal of a stacked target galaxy can be confused with nearby sources due to limitations in telescope spatial resolution ([Jones et al. 2016](#)). This contaminates the recovered average signal and biases the stack, necessitating the use of often substantial corrections (e.g. [Delhaize et al. 2013](#) needed a correction factor of $\times 5$ to account for confusion at $z = 0.1$ using the Parkes 64m telescope). This problem grows as a function of redshift as the projected density of sources in comparison to the beam size increases. Another potential issue is spectroscopic incompleteness of the input source catalogue. For galaxy-by-galaxy H I stacking, and the use of this to recover the dependence of H I on halo mass, this could cause an underestimate of H I group content if gas-rich members are overlooked.

In this work, we look to overcome some of these issues by applying a H I *group*-stacking technique, combining ALFALFA ([Giovanelli et al. 2005](#)) data with optical data from the Galaxy

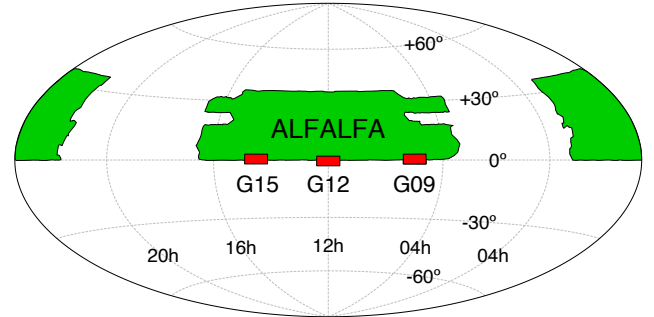


Figure 1. On-sky location of the ALFALFA (green) and the GAMA (red) equatorial regions. The overlap includes a sky area of $\sim 96 \text{ deg}^2$.

and Mass Assembly (GAMA, [Driver et al. 2011](#); [Liske et al. 2015](#); [Baldry et al. 2018](#); [Driver et al. 2022a](#)) survey to derive the dependency of group H I content on halo mass. The group-stacking technique has been previously used in [Guo et al. \(2020\)](#) to calculate the HIHM relation using a combination of ALFALFA and SDSS data. SDSS survey covers $\sim 35\%$ of the sky, and is complete to an apparent r-band magnitude of 17.77mag ([Strauss et al. 2002](#)). On the other hand, the GAMA survey data used in this work is ~ 2 mag deeper but covers a much smaller area. The large overlap between SDSS and ALFALFA makes the final group sample used by [Guo et al. \(2020\)](#) much larger (~ 25000 groups) than the one used here (~ 350 groups). The novelty in this work is the use of GAMA group catalogue, which is deeper and has its group halo masses calculated in a more empirical way using dynamical mass. We also compare our results with simulations and mock observations in this work.

This paper is organised as follows. Section 2 describes the datasets that we are using from the ALFALFA and GAMA survey. In Section 3, we describe our method for extracting the spectra, stacking them and calculating H I mass. The results are presented in Section 4, along with our measurements of the HIHM. In Section 5, we make comparisons with simulations and Section 6 presents our conclusions. Throughout, we assume a Hubble constant of $H_0 = 70 \text{ km s}^{-1} \text{ Mpc}^{-1}$ and a Λ CDM cosmology with $\Omega_M = 0.3$, $\Omega_\Lambda = 0.7$ in calculating distances, comoving volumes and luminosities.

2 DATA

2.1 ALFALFA survey

HI data for this work are taken from the ALFALFA survey, which is a blind HI survey conducted with the single-dish Arecibo telescope using Arecibo L-Band Feed Array (ALFA) ([Giovanelli et al. 2005](#)). ALFALFA survey covered a total area of $\sim 7000 \text{ deg}^2$ out to a redshift of $z = 0.06$. ALFALFA beams are asymmetric Gaussian with Full Width at Half Maxima (FWHM) of $3.8' \times 3.3'$. The ALFALFA grids are 2.4° on each side evenly sampled at $1'$ and the spatial dimensions are 144×144 pixels. ALFALFA data have frequency channel spacing of 24.4 kHz with a spectral resolution of 10 km s^{-1} after smoothing. The average root mean square noise is $\sim 2 \text{ mJy channel}^{-1}$. The complete survey footprint can be split into regions with a common declination of $0^\circ - 36^\circ$ and right ascension

of $07^{\text{h}}30^{\text{m}}-16^{\text{h}}30^{\text{m}}$ and $22^{\text{h}}-3^{\text{h}}$ (see Fig. 1). We use the ALFALFA data cubes from the final data release (Haynes et al. 2018) for this study.

2.2 GAMA survey

GAMA is a spectroscopic survey that was conducted using the Anglo-Australian Telescope, in combination with pre-existing literature measurements. It has resulted in over 300,000 spectroscopic redshifts, covering objects up to a magnitude limit of $r < 19.8$, and extending up to a redshift of $z = 0.4$. The GAMA survey covered 5 separate fields (G02, G09, G12, G15 & G23) on the sky with a total area of $\sim 250 \text{ deg}^2$ and spectroscopic completeness of $\sim 98.5\%$ in the three equatorial fields where most of the GAMA science is done. It also includes several multi-wavelength photometric and imaging surveys of these regions extending from UV to far-IR. The latest GAMA data release—GAMA DR4 (Driver et al. 2022a)—provides complete access to the GAMA spectra, redshifts and other data products. One of these data products is the GAMA Group Catalogue which consists of 26,194 galaxy groups created using the friends-of-friends algorithm of Robotham et al. (2011). The parameters of the algorithm have been extensively calibrated against semi-analytic mock catalogues of the GAMA survey (Merson et al. 2013). The halo masses of the groups are calculated using the velocity dispersion and radius of the group. The halo mass calculation also has been extensively calibrated against the GAMA mock catalogue (Kafle et al. 2016). We use the latest group catalogue (v10 GroupFinding DMU) taken from the GAMA DR4 website¹ for the selection of the galaxy groups studied in this work.

We use the GAMA regions that overlap with the ALFALFA survey, namely G09, G12 and G15 with declination restricted to $> 0^\circ$. We also restrict the group selection to a redshift of 0.06, which is the maximum depth of the ALFALFA survey. The overlap region covers an area of $\sim 96 \text{ deg}^2$ encompassing a volume of $\sim 1.6 \times 10^5 \text{ Mpc}^3$. The ALFALFA and GAMA equatorial regions are shown in Fig. 1.

3 METHODS

3.1 Spectra Extraction

The spectra for the groups are extracted from the ALFALFA data cubes using the group redshift and centre information taken from the GAMA group catalogue. For each group, its H I spectrum is extracted by spatially integrating all the emission inside a radius given by the quadrature sum of group radius (Rad_{100}) and semi-major axis of the beam ($1.9'$) from the group centre, and using a $\pm 1500 \text{ km s}^{-1}$ rest frame velocity range. Rad_{100} is defined as the projected distance from the central group member to the most distant group member converted into angular coordinates and $1.9'$ is the semi-major axis of the ALFALFA beam.

The spectral extraction technique varies depending on whether the object for which the spectrum is being extracted is larger or smaller than the beam size of the telescope. For all our groups, the

spectra are extracted with a radius larger than the ALFALFA beam size. So, the extracted spectrum is given by:

$$S_\nu = \frac{1}{C} \times \sum_x \sum_y S_\nu(x, y) \quad (1)$$

where $S_\nu(x, y)$ is the flux density of each pixel at position x, y and C is a factor correcting from Jy/beam to Jy/pixel (i.e. $C = \text{area of beam/area of pixel}$). The area of the beam is given by:

$$A_{\text{beam}} = \frac{\pi b_{\text{min}} b_{\text{max}}}{4 \ln(2)} = 14.21 \text{ arcmin}^2, \quad (2)$$

where b_{min} and b_{max} are the semi-minor and semi-major axes of the ALFALFA beam. The ALFALFA data are available for two linear polarizations. We perform the spectral extraction for both the polarizations and then take the average of the flux density of both polarizations. For further analysis, we use the polarization averaged spectrum.

3.2 Group Selection

After spectral extraction, we have 501 groups which have overlap between GAMA and ALFALFA. Groups studied in this work have multiplicity of 2 or more ($N_{\text{FoF}} \geq 2$). Halo masses for our groups are taken from the GAMA group catalog (MassAfunc parameter). These are group dynamical masses calculated using group velocity dispersion as given by Eq.18 in Robotham et al. (2011). We only retain groups which have halo mass listed in the group catalogue. For our study, we only use groups with halo masses above $10^{11} M_\odot$ as halo masses below this have larger uncertainties. We also exclude groups that have more than 50% of the data flagged due to Radio Frequency Interference (RFI) in the central region where majority of the H I signal is expected. At the end, we have 345 group spectra on which we perform our study. The distribution of these groups on the sky and as a function of redshift is shown in Fig. 2. The groups are coloured according to their group multiplicities (N_{FoF}) and their size is representative of their group mass in logarithmic scale.

3.3 H I Analysis

3.3.1 Redshift Correction

The extracted spectra are all in the observed frame. So as a first step, we align all the spectra to the rest frequency (1420.4 MHz). This is done by shifting the frequency axis,

$$\nu_{\text{rest}} = \nu_{\text{obs}}(1+z), \quad (3)$$

where ν_{rest} and ν_{obs} are the rest and observed frame frequencies, and z is the redshift of the group taken from the group catalogue. We then convert the flux density to H I mass per unit frequency (referred to as the mass spectrum) (Delhaize et al. 2013),

$$\left(\frac{M_{\text{H I}, \nu_{\text{obs}}}}{M_\odot \text{MHz}^{-1}} \right) = 4.98 \times 10^7 \left(\frac{S_{\nu_{\text{obs}}}}{\text{Jy}} \right) \left(\frac{D_L}{\text{Mpc}} \right)^2, \quad (4)$$

where $S_{\nu_{\text{obs}}}$ is the observed H I flux density and D_L is the luminosity distance of the group. To conserve the total flux or mass, we also scale the mass spectrum appropriately,

$$M_{\text{H I}, \nu_{\text{rest}}} = \frac{M_{\text{H I}, \nu_{\text{obs}}(1+z)}}{1+z}. \quad (5)$$

¹ <http://www.gama-survey.org/dr4/>

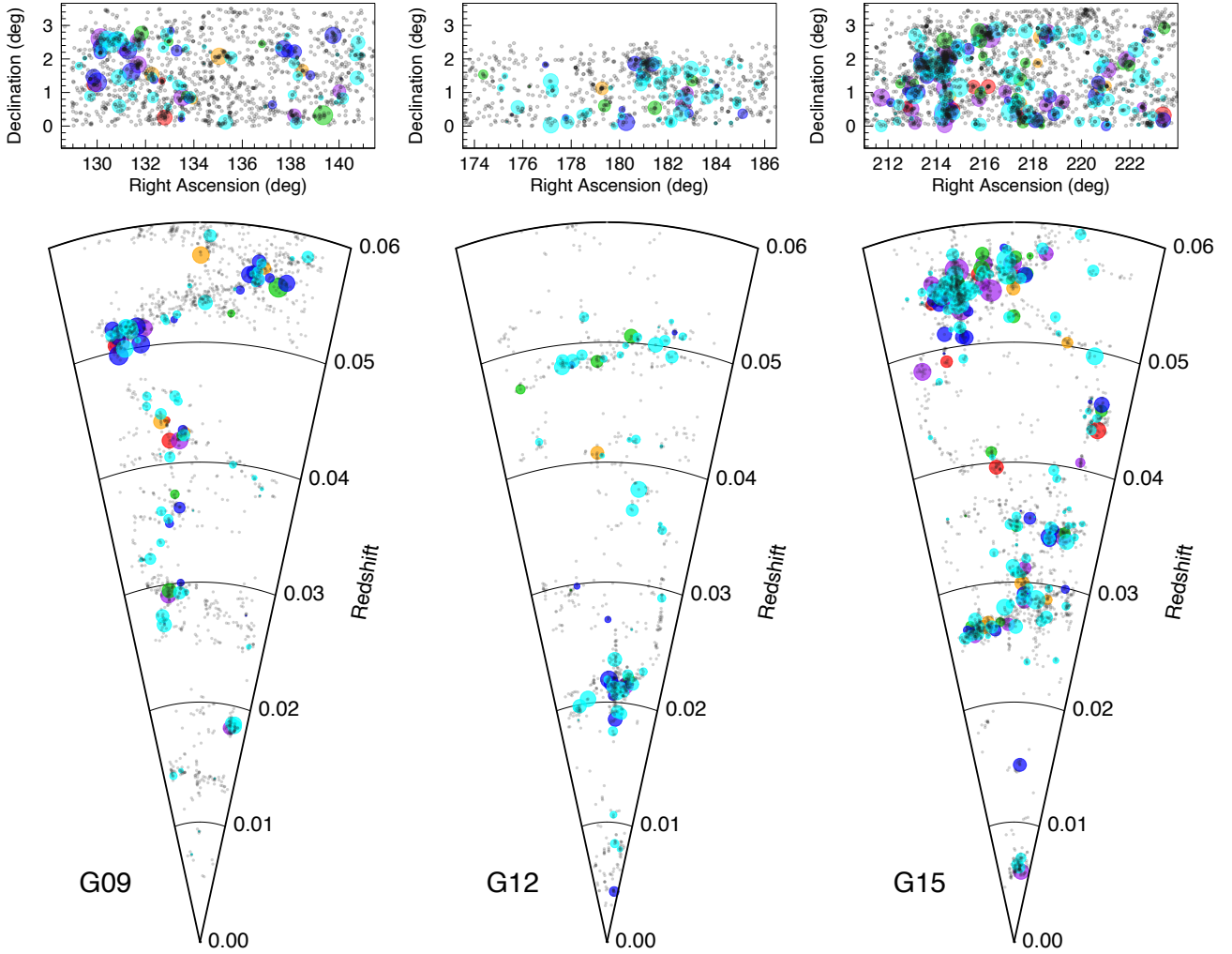


Figure 2. Each panel shows a cone plot of the GAMA groups studied in this work. The groups extend to a maximum redshift of $z = 0.06$ as shown in the lower panel cones. The upper panel shows the distribution of these groups in Right Ascension and Declination. The groups have been colored according to their multiplicities (N_{FoF} with colors "cyan", "blue", "green", "orange", "red" and "purple" indicating multiplicities of 2, 3, 4, 5, 6 and ≥ 7). The circle size denotes the mass of the groups. The individual GAMA galaxies in these fields are shown as grey points.

3.3.2 Baseline Correction

Extracted spectra can have a residual baseline offset from 0, so we perform a baseline correction. [Fabello et al. \(2011\)](#) performs a first order baseline correction in their stacking of ALFALFA galaxies. [Guo et al. \(2020\)](#) also mentions that their ALFALFA group stacks were slightly negative and they performed a second-order polynomial baseline correction. In our spectra, to mark the region where there is potential H I signal, we choose the outermost galaxy member of the group in velocity space with respect to the group centre, then add/subtract a 250 km s^{-1} velocity to it to allow for additional emission spread due to galactic rotation, and mirror this on either side of the spectra centered on the central group member to obtain a symmetric extraction range. This is defined as our group velocity range. We choose 250 km s^{-1} buffer for the spread due to galaxy rotation as it is similar to the rotational velocity of Milky Way-like galaxies ([Eilers et al. 2019](#)). We perform a second order polynomial fit on the part of the spectra outside the group velocity range. After fitting, we interpolate the line within the group region. The total

baseline offset calculated this way is then subtracted from the original spectrum to obtain the baseline-corrected spectrum. For the stacked spectrum, we perform the baseline correction after stacking and not on the individual spectrum. Two examples of baseline correction are shown in Fig. 3 — stacked spectrum (top panels) and direct detection spectrum (bottom panels). On the left panels are the spectrum before baseline correction with the orange line showing the second-order baseline correction which will be subtracted from the original spectrum. On the right panels, we show the baseline corrected spectra. The vertical green lines show the group velocity range.

3.3.3 H I Mass Determination

The H I mass is determined by integrating the H I mass per unit frequency over some channel width,

$$\langle M_{\text{H I}} \rangle = \int_{v_{\text{rest},1}}^{v_{\text{rest},2}} M_{\text{H I}, v_{\text{rest}}} dv_{\text{rest}}. \quad (6)$$

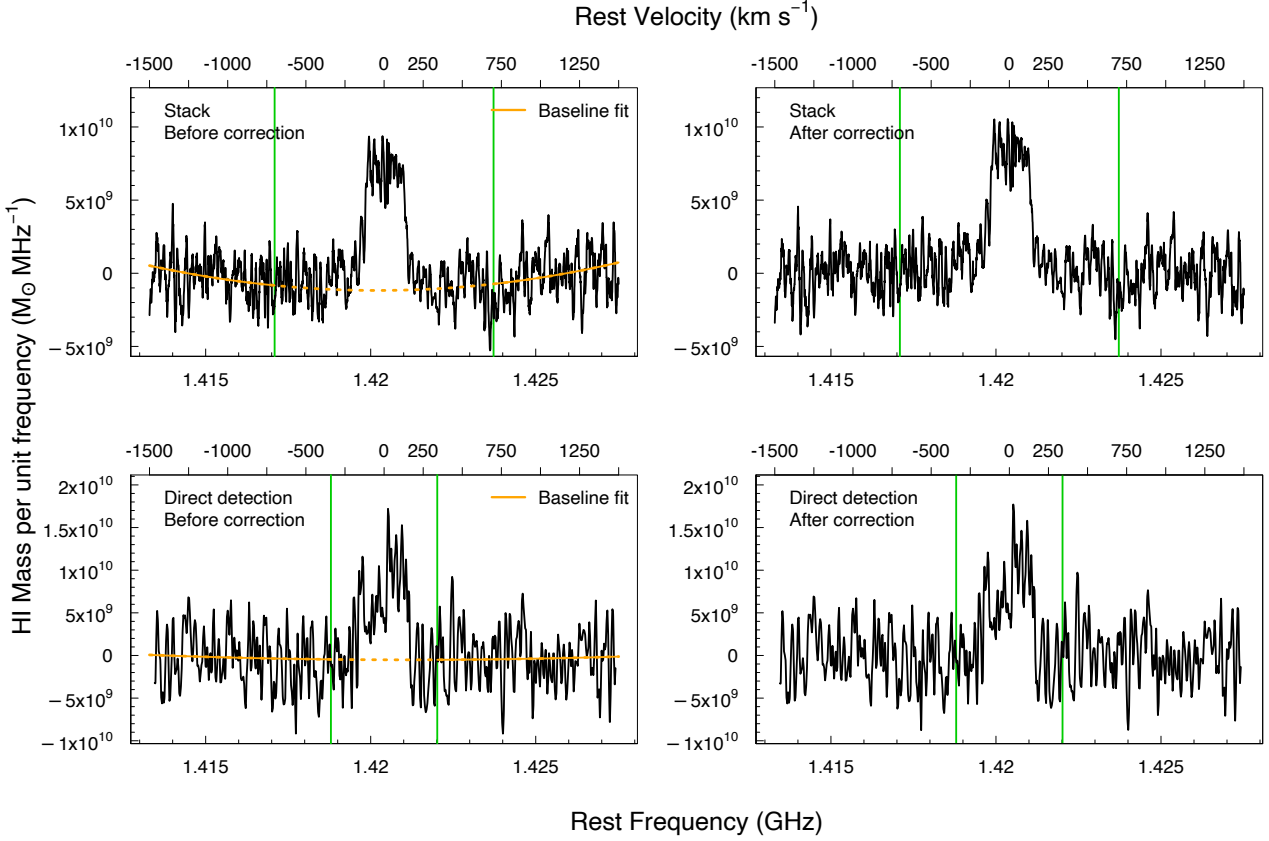


Figure 3. Example of second order baseline correction applied to the group spectra. Baseline correction performed on a stacked spectrum and a direct detection is shown on the top and bottom rows respectively. The green line shows the group velocity range for each spectra and the orange line shows the baseline fit done on the data outside the group velocity range. The fit is interpolated for the region in between the group velocity range.

For the group HI mass, we average the HI mass calculated for increasing widths beyond the group velocity range. We calculate and plot the HI mass for varying group velocity widths, which we call as the curve of growth. This curve is expected to flatten once the HI signal contribution from the group ends and the variations thereafter arise from the noise and background. The curves of growth for all the detections and stacks are shown in Fig. 4. We take an average of the HI mass instead of fixing it at the group velocity width in order to consider the variations in the background and to reduce the impact of our choice on the group velocity width. The curve of growth for detections (black lines) and stacks (coloured lines) are shown in Fig. 4.

3.3.4 Direct Detection

Out of the 345 group, we make a signal to noise ratio (SNR) cut of 3 to classify a group spectrum as being a direct detection. The SNR analysis is performed on the observed flux data using the following equation from Meyer et al. (2017):

$$SNR = \frac{S}{\sigma_{S_{v_{\text{chan}}}} \Delta v_{\text{chan}} \sqrt{N_{\text{chan}}}} \quad (7)$$

where, S is the integrated flux calculated between the group velocity width, $\sigma_{S_{v_{\text{chan}}}}$ is the root mean square flux density error calculated on the spectra excluding the region in between the group velocity

width, Δv_{chan} is the channel width and N_{chan} is the number of channels over which the flux is measured. Any of the group spectra that do not have sufficient data to perform baseline correction is also excluded from being classified as a direct detection. We perform baseline correction for these detections and then calculate their HI masses.

3.3.5 Stacking

Majority of our group HI spectra have low SNR. Hence, we perform stacking to extract the average HI emission. Our stacked spectra includes the contributions from both detections and non-detections. The stacking is done in 5 different halo mass bins — $\log(M_{\text{h}}/M_{\odot}) = 11-12, 12-12.5, 12.5-13, 13-13.5, > 13.5$. These bins have roughly been chosen to have equal number of spectra for stacking (~ 75) in each bin. However, in the last bin, we have lower number of spectra to stack (38) due to the relative rareness of high mass groups. Dividing the groups into five halo mass bins enables us to study the properties of groups in a broader range of environments. Further information about the bin size and number of spectra stacked in each bin are shown in Table 1. For stacking, we first shift all the group spectra to their rest frame using Eq. 5. All the aligned mass spectra are then co-added and averaged with equal weighting applied to each of the spectrum. In many other analysis, inverse-variance weighting is often used (e.g. Guo et al. 2020; Roychowdhury et al. 2022; Rhee et al. 2023). In our case with relatively small numbers of groups in

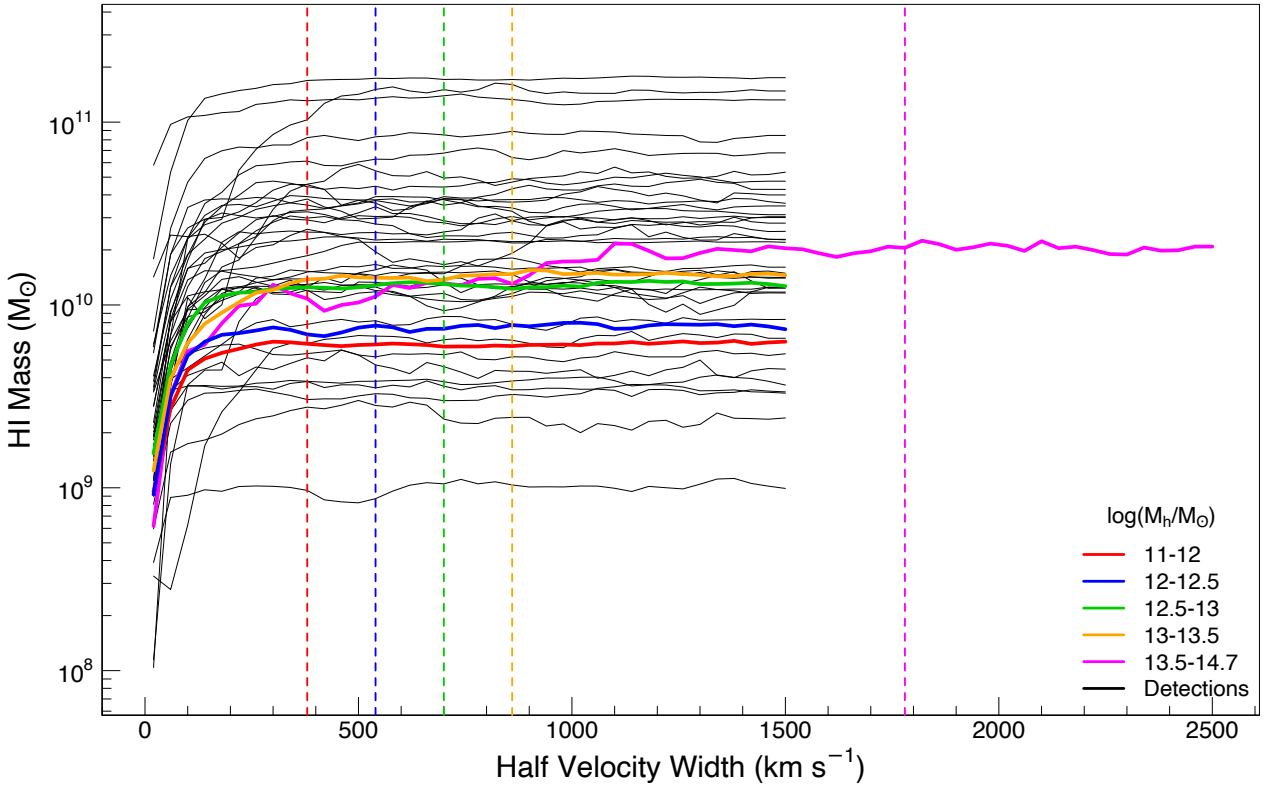


Figure 4. Curve of growth - HI mass as a function of velocity width. In black we show the detections and the stacks of logarithmic halo mass bins 11-12, 12-12.5, 12.5-13, 13-13.5, 13.5-14.7 are shown in red, blue, green, orange and magenta respectively. The vertical colored lines show the group velocity range used for each of the halo mass bin. For all the spectra except the stacked spectrum for the highest halo mass bin, we have spectra extracted over half velocity width of 1500 km s^{-1} . This is the reason all spectra stop at 1500 km s^{-1} and the spectra for the final mass bin extends up to 2500 km s^{-1} .

each halo mass bin, we prefer the equal weighting method so as not to skew the result overly towards a single dominating group. RFI masked regions in every group spectrum is given zero weighting while performing the stacking. To calculate the velocity range for the stacked spectrum, we choose the most outlier galaxy in each halo mass bin, add/subtract 250 km/s and mirror this on either side of the spectra. We then perform the baseline correction on the stacked spectrum and then calculate the HI mass as mentioned earlier (see Eq. 6) for a single group spectrum. The halo mass of the bin is taken as the mean of the halo mass of all the groups in a particular bin that were involved in the stack.

3.4 Error Analysis

The halo mass errors for the direct detections are calculated using the error corrections in [Robotham et al. \(2011\)](#). These are based on the number of group members for each group. The halo mass error decreases with increasing group membership from ~ 1 dex for $N_{\text{FoF}} = 2$ to ~ 0.1 dex for $N_{\text{FoF}} \geq 19$. For the errors in HI mass for direct detections, we include two contributions - the errors arising due to uncertain velocity width and the error due to the noise in the spectrum. First, we look at our HI mass calculation using the curve of growth. Although the curve of growth is supposed to be ideally flat, that is not the case because of background noise. We calculate the 1-sigma variation in the total HI mass by increas-

ing the velocity widths starting from the group velocity range to the end of the spectrum. This is taken as our first error. Next, we try to model the effect of noise in our spectrum. For this, we recreate each detection group spectra by adding a random noise to the flux at each channel which is calculated by sampling from a uniform distribution with mean 0 and standard deviation as the root mean square error of the spectrum. We then recalculate the HI mass for the new spectra. This is repeated 1000 times and the standard deviation from this is taken as the second error. These two errors could be correlated, but we follow the conservative approach and add the errors in quadrature to get the final HI mass error for detections.

For the stacks, we perform a Monte-Carlo (MC) analysis by recalculating the halo mass for each of the 345 groups from a normal distribution with mean equal to the GAMA group halo mass and standard deviation equal to the halo mass error. This can result in groups moving into different halo mass bins. We now recalculate our full stacking analysis with the new set of halo mass bins and calculate the HI masses and mean of the new halo mass bins. This is repeated 1000 times. The standard deviation from these 1000 iterations is taken as the error for our HI mass and halo mass in each bin.

We use our MC analysis to quantify and correct for Eddington bias in our data. Eddington bias arises due to the steepness in the Halo Mass Function combined with the large errors in our halo masses tending to scatter more low mass halos towards high than

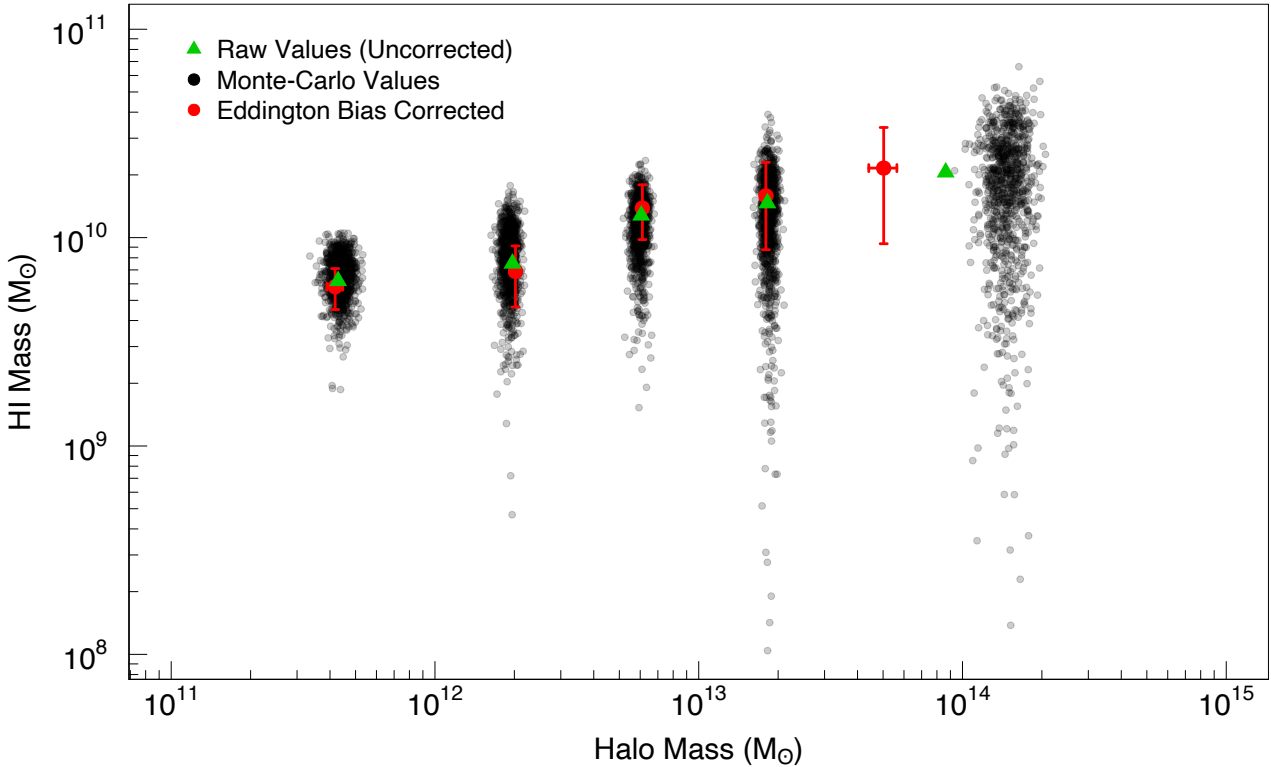


Figure 5. Monte Carlo analysis of our group stacking. The raw HIHM values for each halo mass bin is shown in green. In black, the 1000 Monte-Carlo sampled values are shown. The Eddington bias corrected points are shown in red. We can see that significant Eddington bias is only present in the highest mass bin.

the opposite. We use the Eddington bias correction approach used in [Driver et al. \(2022b\)](#). The results for the Eddington bias correction applied for each mass bin is shown in Fig. 5. Here, we define the difference between the raw value and mean of the MC values as the Eddington bias correction factor. The raw values refer to the HI mass calculated for the original stacked spectra and these are shown by the green triangles. The black circles show the 1000 MC iterations performed by resampling the halo mass of the groups within their errors. Eddington bias correction factor for each halo mass bin is then the difference between the green triangle and mean of the distribution of black points. We subtract this factor once again from the raw values to obtain the original Eddington bias corrected values shown by red dots with errors. The errors are given by the 1σ distribution of the black points. The offset between the red, green and black points show the extent of the Eddington bias at each halo mass bin. The first 4 bins do not show a large Eddington bias whereas the bias is significant for the highest mass bin. The large Eddington bias we see in our highest mass bin arises because the “knee” of the halo mass function lies within this bin with a characteristic mass of $\log_{10}(M_h/M_\odot) = 14.13^{+0.43}_{-0.40}$ ([Driver et al. 2022b](#)). Hence, far more halos are moved across the knee to high mass than vice versa. We could tighten the upper bound of the bin to mitigate the biases but choose not to due to the already small number of groups in this bin. Note that in these bins we measure the mean halo mass and find that the median has a similar but slightly lower Eddington bias value. The assumption in our Eddington bias correction approach is that the correction factor between first order (difference between

red and green point) and second order (difference between green and black points) Eddington bias is the same. We also perform a jack-knife analysis in each halo mass bin to estimate the HI mass error, however we note that this error is subdominant compared to the error from the MC analysis. Hence, for our final stack results, we only use the error from MC analysis.

4 RESULTS

4.1 Direct Detections

Based on our SNR cut and group selection, we classify 37 groups out of 345 as being a direct detection. Spectra for 4 of these 37 groups are shown in Fig. 6. All the spectra are shown in the rest frame HI velocity space of the central group member. Plotted as vertical red lines are the spectral locations of the group members based on their optical redshifts from GAMA catalogue. We follow the steps described in Section 3.3 to calculate the HI mass for each of these groups. The curves of growth for all the detections are shown in Fig. 4 in black. In Fig. A1, we have shown the spectra for all 37 groups having direct detections and the properties of each of these are given in Table A1.

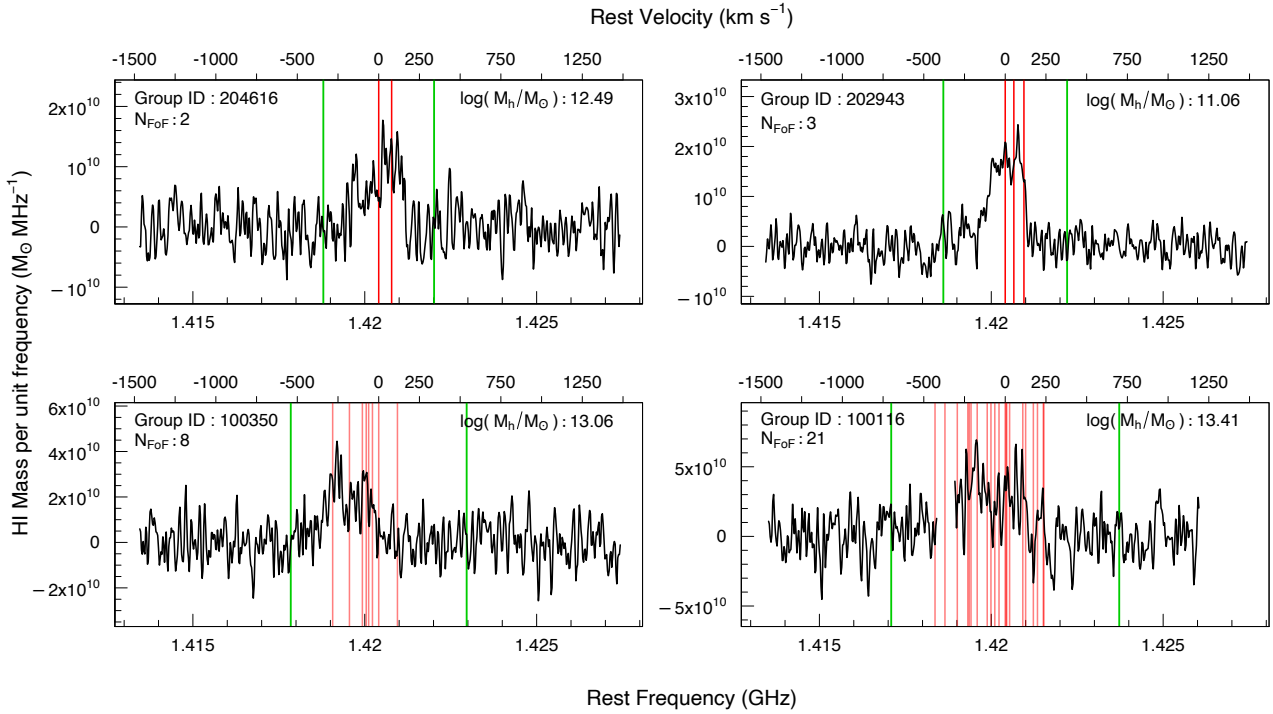


Figure 6. Spectra of 4 (out of 37) groups which have direct detections based on a SNR cut of 3 are shown here. All the spectra have been shifted to the rest frame. The GAMA Group ID, number of group members and halo mass of the group is shown in each panel. The positions of various group members are shown in red. We show the all the 37 direct detection spectra in Fig. A1.

Halo Mass Bins	Number of Groups	$\log_{10}(\text{Halo Mass}/M_{\odot})$	$\log_{10}(\text{H I Mass}/M_{\odot})$
[11.0, 12.0)	79	11.62 ± 0.03	$9.76^{+0.10}_{-0.11}$
[12.0, 12.5)	77	12.30 ± 0.02	$9.84^{+0.14}_{-0.19}$
[12.5, 13.0)	78	12.79 ± 0.02	$10.14^{+0.14}_{-0.15}$
[13.0, 13.5)	73	13.25 ± 0.02	$10.20^{+0.18}_{-0.34}$
[13.5, 14.7)	38	13.70 ± 0.05	$10.33^{+0.19}_{-0.37}$

Table 1. Group stacking results after Eddington bias Correction. Column 1 - Halo Mass bin, 2 - Number of spectra used in the stack, 3 - Mean Halo Mass of all the groups in the bin expressed in log units, 4 - H I mass of the stacked spectrum expressed in log units.

4.2 Stacking Results

The stacked spectra in 5 different halo mass bins is shown in Fig. 7. There is a clear signal in all five bins. The halo mass of the groups range from $M_h/M_{\odot} = 10^{11}$ to $10^{14.7}$. H I mass and halo mass values for all the individual bins are shown in Table 1. The width of the stacked spectrum increases with increasing halo mass, as expected, because the velocity dispersion are higher for groups with more massive haloes. This is also directly visible in the increasing spread of red vertical bands with increasing halo mass bin. The spectrum of the highest mass bin ($= 10^{13.5} - 10^{14.7} M_{\odot}$) is relatively more noisy. This bin also has the least number of spectra stacked compared to the other 4 bins, mainly due to the diminishing number of high mass groups. For our groups in the highest halo mass bin, we extracted the spectra with a larger velocity range (± 2500 km/s) compared to groups in other bins (± 1500 km/s). This is done because the velocity width range for the highest mass bin is more than ± 1500 km s^{-1} as can be seen in Fig. 7. We also perform a control stack in each of the halo mass bin. For this, we randomize the velocity of each group

member and perform the stacking. This should result in a noisy spectra without any signal. The control stacked spectrum for each halo mass bin is shown with the grey line in Fig. 7.

4.3 The HIHM Relation

In Fig. 8, we plot the HIHM relation for our set of groups, both direct detections (red) and stacks (black). The stacked points are shown after Eddington bias corrections. Literature values from Guo et al. (2020), Obuljen et al. (2019), Li et al. (2022) and Rhee et al. (2023) are shown. In the HIHM plot, the detections seem to be located above the stacks and this is expected given the detections represent the most H I rich groups for a given halo mass. Hence, the stacks represent the more average H I content for a group in a particular halo mass range by construction. For the stacks, the H I mass increases with halo mass and seems consistent with a power law. Considering the large errorbars, it can also be argued that the HIHM relation seems to flatten towards the high-mass end. We see

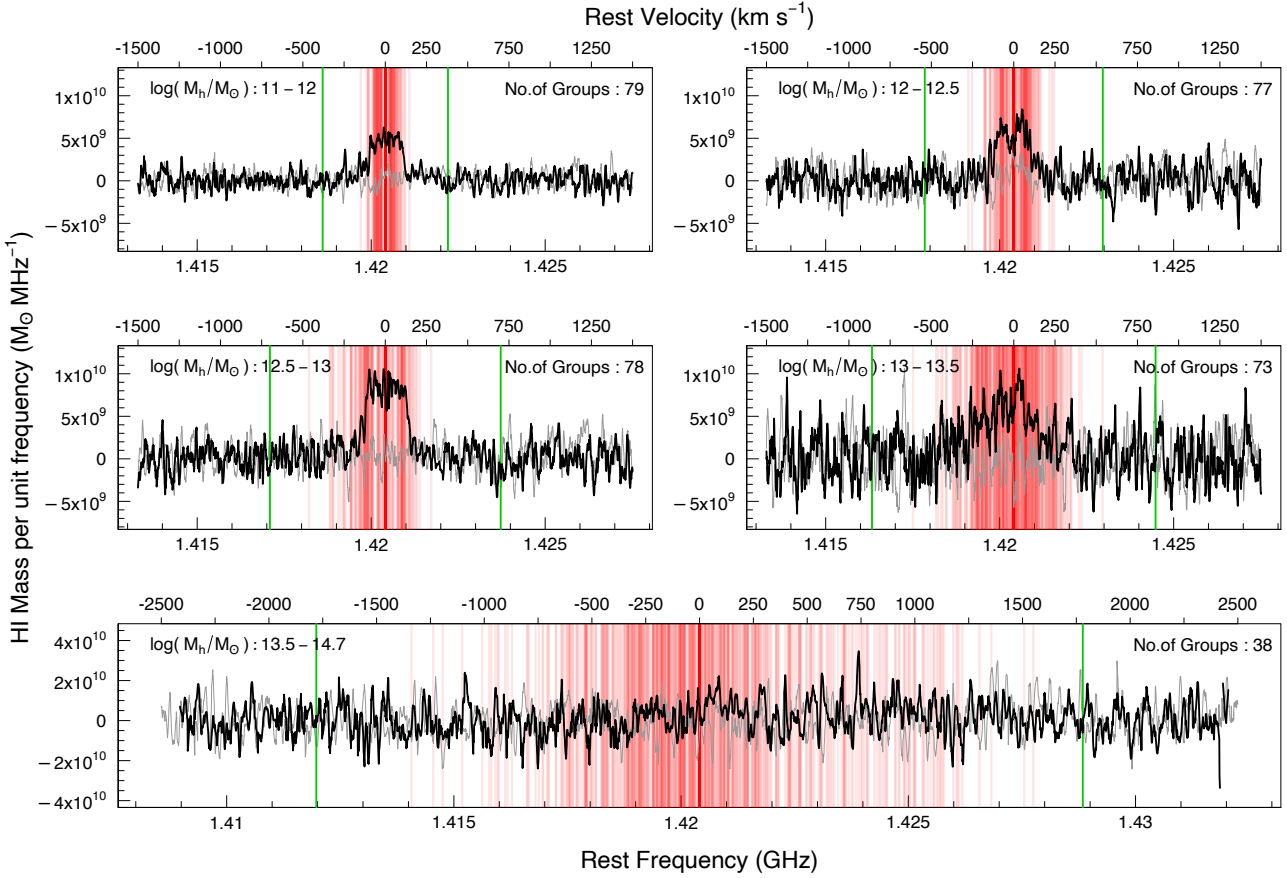


Figure 7. Stacks for the GAMA groups in halo mass bins. The green line shows the group velocity width of the stacked spectra. On the top side of each panel the halo mass range of the stack and the number of groups used for that stack are mentioned. In red lines, the position of each group member is shown. The groups in the highest halo mass bin have been extracted and stacked over a wider frequency range (± 2500 km s $^{-1}$) because of its larger group velocity range compared to other 4 bins. In grey, we show a control spectra for each bin where the stacking was performed by randomizing the velocities of each group member.

that the average group H I content is 1.3% of the halo mass at the lowest mass bin and it comes down to 0.4% of the halo mass at the highest bin.

Our HIHM results for the stacks is consistent with the results of Guo et al. (2020) across all the halo mass bins. Guo et al. (2020) obtained their HIHM relation using a H I group spectral stacking technique similar to the one used in this work. Their H I data was also from ALFALFA, but the group catalogue is based on SDSS data. The halo masses from the Lim et al. (2017) group catalogue used by Guo et al. (2020) are proxy-masses estimated based on the stellar mass-halo mass relation. This is very different from the mass estimates in GAMA group catalogue (Robotham et al. 2011) which corresponds to dynamical halo mass estimates which are calculated using group velocity dispersions. Despite the smaller sample and a different group catalogue, the agreement between our study and Guo et al. (2020) is very good. We have large error bars on our stacked results due to the relatively small group sample used in our stacking along with the implementation of an extensive Monte-Carlo for error analysis. We clarify that these errors are uncertainties on our group-stacking results and do not represent the scatter in HIHM relation.

Rhee et al. (2023) calculated their HIHM relation (shown in brown in Fig. 8) using the DINGO early-science data and GAMA group catalogue. H I spectra of individual galaxies from groups belonging to common halo mass bins were stacked to calculate the

HIHM relation. This is a galaxy-based stacking whereas in our work we do a group-based stacking. Galaxy-based stacking does not take into account the contributions from any H I gas that are unbound to galaxies in the intra-group medium. This would also miss out on the H I in galaxies that are below the detection limit of GAMA. Hence, the resultant HIHM relation in Rhee et al. (2023) would be considered as a lower limit. It can be argued that our derived group HI masses could be overestimated. The group-stacking technique tries to include all the H I in groups but on the other hand these could also be contaminated by interlopers (Chauhan et al. 2021).

In Fig. 8, we show data from Li et al. (2022) in blue. Li et al. (2022) creates a new H I mass estimator where four different galaxy properties—surface stellar mass density, color index, stellar mass and concentration index—are used to model H I-to-stellar mass ratio. This estimator is calibrated with the xGASS sample (Catinella et al. 2018) and then used to calculate H I mass functions. The final HIHM relation shown in blue is estimated from Lim et al. (2017) group catalog. The H I mass of each group member is calculated using their estimator and summed up to get the total H I mass of a group. All the groups have been divided into halo mass bins to get the final HIHM relation. The Li et al. (2022) results fall below our data at the lowest halo mass bin but predicts more H I in the highest halo mass bin. The disagreement could be attributed to the modified H I mass estimation technique used in Li et al. (2022) compared to the spectral stacking used in this work. It is also important to

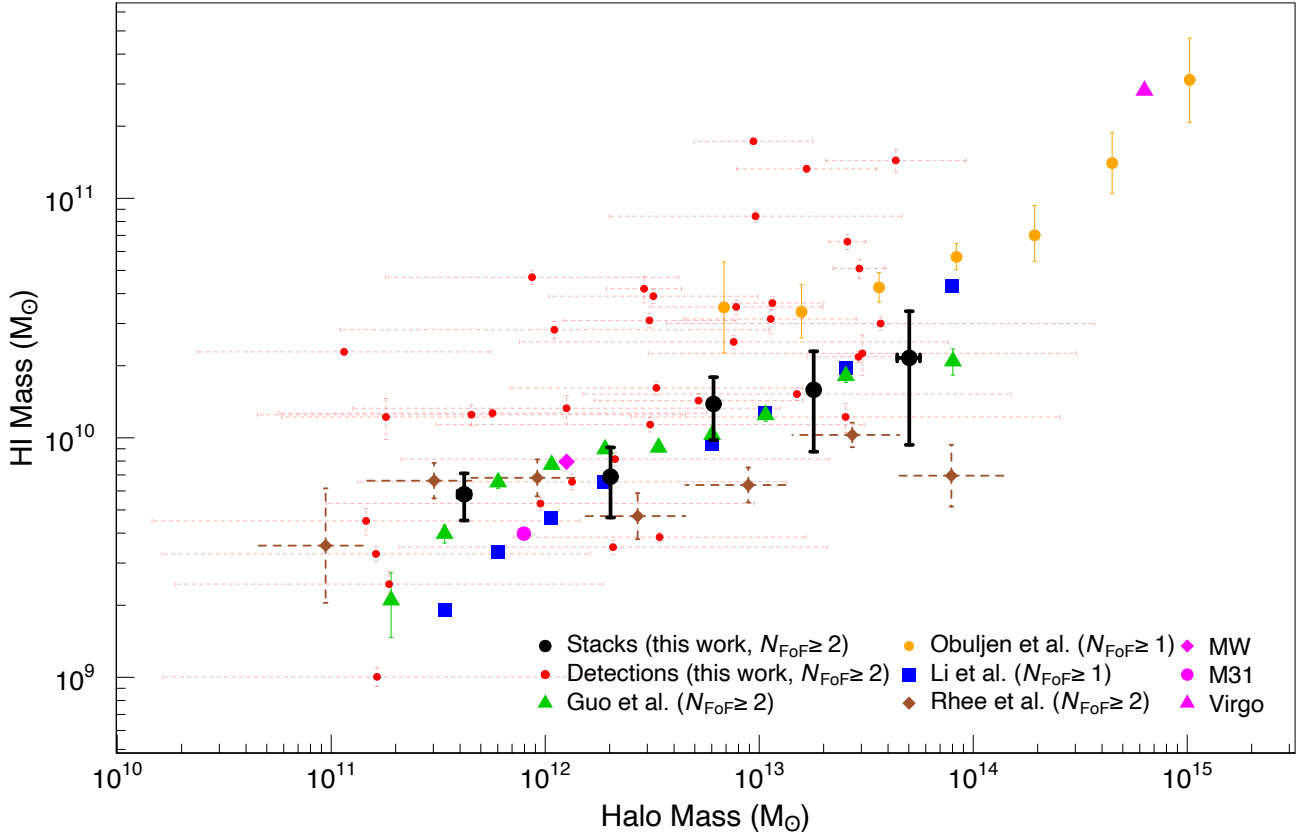


Figure 8. HI-to-Halo Mass Relation for our Group Stacks in halo mass bins as well as individual group detections compared with other observational studies. The stacked groups are shown in black with the error bars calculated using a Monte-carlo Analysis. These points have Eddington bias corrections applied to them. In general, we see an increasing trend in the H I mass as a function of halo mass. The individual group detections are shown as red points. We display the data from Guo et al. (2020), Obuljen et al. (2019), Li et al. (2022) and Rhee et al. (2023). Our method of group H I stacking is most similar to the analysis done by Guo et al. (2020) and we agree well with their trend within the errorbars. Obuljen et al. (2019) & Li et al. (2022) results are for $N_{\text{FoF}} \geq 1$ and the rest are for $N_{\text{FoF}} \geq 2$. We also show the MW, M31 and Virgo measurements from literature.

note that the group membership (N_{FoF}) in Li et al. (2022) includes $N_{\text{FoF}} \geq 1$, which can also be the reason for disagreement especially at the lowest mass end because our sample includes groups with $N_{\text{FoF}} \geq 2$.

In orange, we have plotted the data from Obuljen et al. (2019), which uses a similar dataset as the Guo et al. (2020) i.e. ALFALFA and SDSS. However, Obuljen et al. (2019) also does not directly measure the group H I masses but instead it is calculated by integrating the HIMF at various halo masses. Their HIMF mass function is calculated using a 2D stepwise maximum likelihood estimator. Obuljen et al. (2019) probes the high halo mass regime ($\sim 10^{13}$ - $10^{15} M_{\odot}$). For the halo masses where our study overlaps with Obuljen et al. (2019), we see that their H I masses are systematically higher by ~ 0.3 - 0.5 dex. This could either be because they have systematically overestimated the HIMF for each halo mass, or because of a steep low-mass slope leading to an overestimate while integrating the HIMF. Alternatively, our direct stacking measurements may still be missing very low-mass HI that might have been accounted for in the HIMF. This analysis again includes groups with $N_{\text{FoF}} \geq 1$ which could bias the comparisons with our results, although the fraction of groups with only one member at the high halo mass end is expected to be low.

We also show the position of Milky Way (MW), Andromeda

(M31) and Virgo cluster in H I-halo mass plane. The halo masses of MW (Piffi et al. 2014) and M31 (Kafle et al. 2018) have been calculated by mass modelling based on the escape velocity of stars or planetary nebulae. The Virgo halo mass is taken from Kashibadze et al. (2020). The H I masses of MW, M31 and Virgo are taken from Kalberla & Kerp (2009), Chemin et al. (2009) and Li et al. (2022) respectively.

5 COMPARISON WITH GALAXY FORMATION SIMULATIONS

We compare the HIHM relation observed by us versus that predicted by the simulations in Fig. 9. We use the IllustrisTNG hydrodynamic simulation (Nelson et al. 2018; Pillepich et al. 2018) and SHARK semi-analytical model of galaxy formation (Lagos et al. 2018). The HIHM relation has been studied previously using simulations (e.g. Villaescusa-Navarro et al. 2018, Spinelli et al. 2020; Baugh et al. 2019; Chauhan et al. 2020). However, at face value, there is significant variance between different models. The dotted lines in Fig. 9 show the HIHM relation from the fiducial results of TNG (Villaescusa-Navarro et al. 2018), referred to as ‘TNG-ref’ hereafter, in green, and SHARK (Chauhan et al. 2020), referred to as

	Group membership	Halo mass definition	Boundary definition for H I mass	Includes intra-halo H I	Lightcone	Occupancy
Observations (this work)	Galaxy FoF (Robotham et al. 2011)	Dynamical (Robotham et al. 2011)	$R_{2D} = \text{Rad}_{100} + 1.9'$ $ \Delta v < v_{\text{max}} + 250 \text{ km s}^{-1}$	Yes	N/A	$N_{\text{FoF}} > 1$
SHARK-mock 1	Galaxy FoF (Robotham et al. 2011)	M_{200c} from abundance matching	$R_{2D} < 2R_{200c}$ $ \Delta v = v_{\text{vir}} - 2 \times v_{\text{vir}}$	No	Yes	$N_{\text{FoF}} > 1$
SHARK-mock 2	Galaxy FoF (Robotham et al. 2011)	Dynamical (Robotham et al. 2011)	$R_{3D} < R_{200c} - 2 \times R_{200c}$	No	Yes	$N_{\text{FoF}} > 1$
SHARK-ref	Particle FoF	M_{200c} from FoF	$R_{3D} < R_{200c}$	No	No	$N_{\text{FoF}} > 0$
TNG - mock	Particle FoF	Dynamical (Robotham et al. 2011)	All FoF H I	Yes	No	$N_{\text{FoF}} > 1$
TNG - ref	Particle FoF	M_{vir} from FoF (Bryan & Norman 1998)	All FoF H I	Yes	No	$N_{\text{FoF}} > 0$

Table 2. Comparison of various simulations and mocks with our observational data. Column 1 - Dataset; Column 2 - indicates how the group membership is defined; Column 3 - halo mass definitions used; Column 4 - indicates the boundary which was used to calculate the H I mass; Column 5 - Indicates whether intra-halo H I would be included in the total H I estimation; Column 6 - Indicates whether mock lightcone was used to for the simulation; Column 7 - Indicates whether the groups include single occupancy halos or not.

‘SHARK-ref’ hereafter, in purple. On the other hand, different observational studies can also differ in their final results. Galaxy group catalogues built from different surveys usually have different magnitude limits, completeness and hence might miss out on the low magnitude galaxies. Halo mass measurement also varies for different group catalogues, e.g. GAMA group catalogue uses a dynamical mass estimation (Robotham et al. 2011), while abundance-matching estimates are used for SDSS-based group catalogues (Yang et al. 2005; Lim et al. 2017). Therefore, in order to fairly compare the results from observations and simulations, it is necessary to first create mock observations from the same simulations. In Table 2, we provide a comparison between the observation, simulation and mocks in terms of how the groups are defined, the halo mass definition used, the group boundary criteria, whether H I in the intra-halo medium is included, whether lightcones were used to generate the simulations and the minimum number of group members.

We compare our results against mock-observational results from SHARK (Chauhan et al. 2021), hereafter ‘SHARK-mock’. These were created from a GAMA-like mock lightcones, applying an ALFALFA survey selection to it. Chauhan et al. (2021) ran the same Robotham et al. (2011) group finder on the mock lightcone, which allowed them to make a one-to-one comparison with stacking measurements made using FoF-like group finders. Chauhan et al. (2021) extensively looked at various systematics involved in H I stacking measurements such as the effects of different apertures, velocity widths and halo mass estimators. It is important to note here that, mock stacking as referred to in Chauhan et al. (2021) does not involve actual H I spectral extraction of groups and averaging them. All the H I in galaxies within each group as defined by the halo-finder are fully detected and their values are averaged to obtain the H I mass in a given halo mass bin. In Fig. 9, as a blue band, we show the HIHM relation from the SHARK-mock 1, where the group stacking was performed with an adapting group velocity width range that varied depending on the halo virial velocity (adapted from fig. 10 in Chauhan et al. 2021). The H I masses were calculated by doing a forward-modelled H I stacking that resembles the realistic geometrical stacking. However, the halo masses in this case were obtained from abundance matching and hence are different from the dynamical halo masses in our stacks. The large scatter between abundance or dynamically estimated masses against the true halo

masses in SHARK can be seen in fig. 4 of Chauhan et al. (2021). Dynamical mass estimates would make the relation flatter especially at the low halo mass end. This is shown by the purple shaded region in our Fig. 9, SHARK-mock 2, where the halo masses are dynamical masses. However, the H I mass in this case are not from mock stacking but instead the mean H I content of groups identified by the group finder (adapted from fig. 6 in Chauhan et al. 2021). SHARK-mock 2 groups are defined by a spherical aperture around the central galaxy instead of a projected aperture. The ideal comparison to our results would have been a combination of the two SHARK mocks with dynamical halo masses and realistic mock stacking to derive the H I content. Excluding the initial point, our measurements are consistent with the SHARK-mock 1 but have a systematic disagreement with SHARK-mock 2. The reason for the deviation between SHARK-mock and SHARK-ref above $10^{12} M_{\odot}$ is also attributed to the large scatter between halo masses estimates in this region, thereby washing out any dip-like feature of the HIHM in SHARK-mocks that can otherwise be seen in SHARK-ref (Chauhan et al. 2021).

For the Illustris TNG simulation, we conduct a different procedure that helps us to mimic some of the selection functions we have in the observations, but we caution that we do not build lightcones or run group finders in this case, as was done in Chauhan et al. (2021) for SHARK; such an analysis is very involved and beyond the scope of this paper. We refer to this as ‘TNG-mock’. For this, we first select Friends-of-friends (FoF) groups with at least 2 galaxies from the TNG100 simulation (Nelson et al. 2018; Pillepich et al. 2018) with a stellar mass cut of above $10^{8.5} M_{\odot}$. The galaxies were extracted from a pre-constructed dataset of TNG100 galaxies at $z = 0$ with total gas OR stellar masses above $10^9 M_{\odot}$ and DM fractions above 5% (the same dataset used in Davé et al. 2020). The selection is not done based on luminosities, which is what would ideally be done with a GAMA-like FoF group finder. The H I masses of the groups were computed using all gas cells in each FoF group. Our calculation of the H I mass of haloes differs to Villaescusa-Navarro et al. (2018) (shown as green dotted line in Fig. 9) in that we have included the updated H I / H₂ modelling from Diemer et al. (2018) and Stevens et al. (2019), using the prescription based on Gnedin & Draine (2014). The main differences are the improved modelling of the UV field in each halo, which accounts for local sources from star formation, and the application of a different

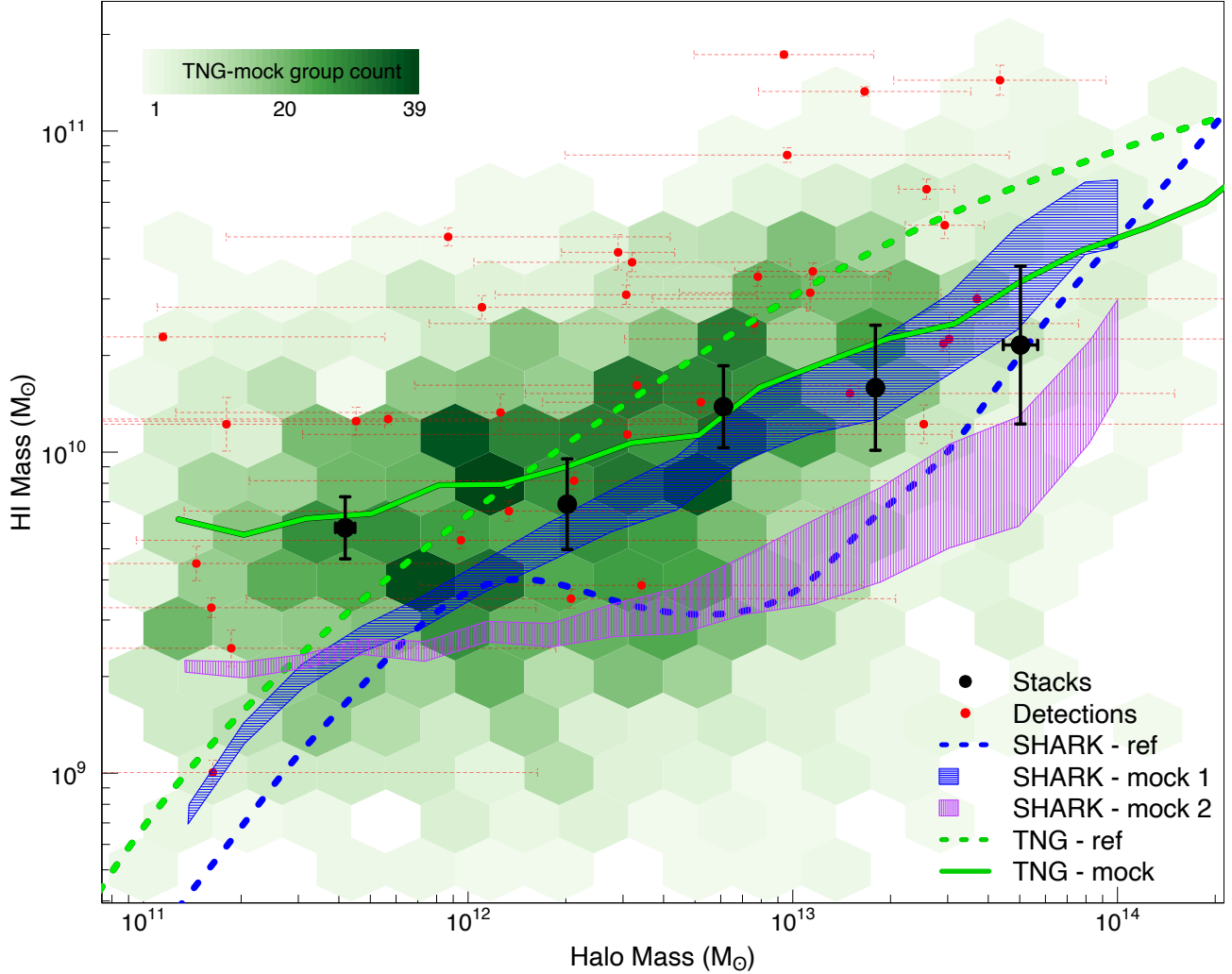


Figure 9. HIHM Relation for our Group Stacks and Direct Detections compared with simulation results from SHARK (blue) and Illustris TNG (green). The dotted lines represent the raw simulation outputs (Villaescusa-Navarro et al. 2018; TNG-ref; Chauhan et al. 2020; SHARK-ref). The solid lines show mock observations created from the simulations, which are better suited for comparison with our data. Mock SHARK observations were taken from Chauhan et al. (2021). The mocks in this case are fully-forward modelled, having simulated a GAMA and ALFALFA sky and having run the Robotham et al. (2011) group finder. SHARK-mock 1, shown by the blue shaded region, calculates HI mass in a similar manner to our work, but using a larger radius and with a varying velocity window. The halo mass definition, however, is based on abundance matching, and therefore is different to our data. In SHARK-mock 2, shown by the purple shaded region, the opposite is true; that is, halo mass is defined the same way as in our results, but the HI masses are a direct sum of the known HI masses of the simulated group members. Mock TNG results, shown with green hexagons, were created by selecting FoF groups with 2 or more members, and HI masses were computed with the improved HI / H₂ modelling developed in Stevens et al. (2019). The halo masses are dynamical masses, calculated in a similar way as the GAMA group catalogue, but the halo catalogue has not been modified from the public one. The running mean of the TNG mock is shown by the solid green line; this can be fairly compared with our results and shows remarkable agreement. Note that, while TNG-mock is not fully forward modelled as the SHARK-mock, selection cuts were made to be consistent with GAMA and ALFALFA. We show our 37 direct group detections in red and in green hexagons we show the distribution of the TNG-mock groups in the HIHM plane. The darker hexagons correspond to higher number of groups in a given hexbin. The location of direct detections on the HIHM plot, although naturally biased higher than the stacks as these would be more HI-rich, is in agreement with the distribution of TNG groups.

prescription for how the UV and presence of metals/dust affects the molecular/atomic equilibrium. We have also excluded haloes occupied by a single galaxy to match the group definition of GAMA. To make a fair comparison between our results and TNG100, we recompute the simulation's halo masses to be consistent with the dynamical method of Robotham et al. (2011) used for the GAMA groups. While less ideal, we maintain the FoF group definition as in the public TNG data. The location of these TNG-mock results on

the HIHM plot is shown by the green 2D histogram in Fig. 9 with darker hexbins corresponding to higher number of groups, and we have calculated a running mean shown as solid green line. The mean HIHM relation from the TNG-mock is consistent with our group stacking results. The reason for the deviation between TNG-mock and TNG-ref is due to the different halo mass definitions. We also plot our direct detections in Fig. 9 as red circles. The distribution of

our direct detections is in agreement with the distribution of groups in the TNG-mock as shown by the 2D histogram.

Our overall analysis is largely restricted to halo mass below $\sim 10^{14}M_{\odot}$ thereby not enabling a proper comparison in the cluster regime. Obuljen et al. (2019) and simulations (Chauhan et al. 2020; Villaescusa-Navarro et al. 2018) suggest an increasing trend of the group HI masses even beyond $10^{14}M_{\odot}$. The better consistency of our results with the mock observations compared to simulations' fiducial results, highlights the importance to create mock catalogues for a fairer comparison between the observations and simulations. The comparisons do show that the way the mocks are observed also affects the resulting HIHM relation (Chauhan et al. 2021). The significant agreement between our data and the predictions of two simulations, which utilized different computational methods, assumptions, and baryon physics implementations, but both based on Λ CDM, is yet another example of the success of the standard cosmological model.

6 CONCLUSIONS

In this paper, we have calculated the HI content of galaxy groups in the overlap region of ALFALFA and GAMA surveys. We have used the GAMA group catalogue to determine the location and halo mass of the groups. After spectral extraction and cleaning, we have 345 groups in a halo mass range from $10^{11}M_{\odot}$ - $10^{14.7}M_{\odot}$ on which we perform our analysis. From the individual group spectra, we have obtained 37 direct detections with $\text{SNR} > 3$. We divide the 345 groups into 5 halo mass bins (see Table 1) and perform the stacking analysis in each bin. We also perform an Eddington bias correction on our stacked results. Eddington bias is prominent only in the highest mass bin.

We look at the HIHM relation for our direct detections and the stacks. The direct group detections are naturally biased to have higher HI masses at a given halo mass than the stacks. But, we see that the location of these direct detections on the HIHM plane is consistent with the mock observations done with TNG. We see an increasing trend of HI mass as a function of halo mass with some indication of flattening towards the higher halo mass end. The average HI mass content changes from 1.3% of the halo mass at $10^{11.62}M_{\odot}$ to 0.4% at $10^{13.70}M_{\odot}$. We compare our HIHM measurements with previous studies. We find that our results are consistent with the HI group stacking measurements of Guo et al. (2020). Despite the differences in group catalogues, survey detection limits as well as the halo mass measurement techniques between our work and Guo et al. (2020), the results agree across the entire halo mass range. We do find differences with Li et al. (2022) and Obuljen et al. (2019) at the lowest and highest halo mass bins. This could be due to systematic bias in the way the HIHM relation has been calculated in the two studies. We compare our results with simulations and mock observations of SHARK and TNG. We see that our results are fairly consistent with mock observations and point out that it is essential to create mock observations when making comparisons with theoretical studies. Since, we do not probe the cluster regime in this study, we need future studies of high-mass groups to validate these results. Deeper and more sensitive HI surveys such as DINGO on Australian Square Kilometre Array Pathfinder (ASKAP, Johnston et al. 2007, 2008; Hotan et al. 2021) and the HI emission project within the MeerKAT International GigaHertz Tiered Extragalactic Exploration (MIGHTEE-HI, Jarvis et al. 2016; Maddox et al. 2021) survey on the Meer-Karoo Array Telescope (MeerKAT,

Jonas & MeerKAT Team 2016) will enable improved studies of the HI-to-halo mass relation.

ACKNOWLEDGEMENTS

We thank the referee for the thorough reading of our work and the constructive feedbacks. GAMA is a joint European-Australasian project based around a spectroscopic campaign using the Anglo-Australian Telescope. The GAMA input catalogue is based on data taken from the Sloan Digital Sky Survey and the UKIRT Infrared Deep Sky Survey. Complementary imaging of the GAMA regions is being obtained by a number of independent survey programmes including GALEX MIS, VST KiDS, VISTA VIKING, WISE, Herschel-ATLAS, GMRT and ASKAP providing UV to radio coverage. GAMA is funded by the STFC (UK), the ARC (Australia), the AAO, and the participating institutions. The GAMA website is <http://www.gama-survey.org/>. Based on observations made with ESO Telescopes at the La Silla Paranal Observatory under programme ID 179.A-2004. Based on observations made with ESO Telescopes at the La Silla Paranal Observatory under programme ID 177.A-3016. We gratefully acknowledge DUG Technology for their support and HPC services.

This work is based on ALFALFA survey conducted with the Arecibo Observatory. We acknowledge the work of the entire ALFALFA team for providing us access to their data cubes.

Part of this research was supported by the Australian Research Council Centre of Excellence for All Sky Astrophysics in 3 Dimensions (ASTRO 3D) through project number CE170100013.

ARHS is a grateful recipient of the Jim Buckee Fellowship at ICRAR-UWA. CL has received funding from the ASTRO 3D, through project number CE170100013, and the Australian Research Council Discovery Project (DP210101945). DO is a recipient of an Australian Research Council Future Fellowship (FT190100083) funded by the Australian Government.

DATA AVAILABILITY

The data underlying this article will be shared upon reasonable request to the corresponding author, AD.

REFERENCES

- Baldry I. K., et al., 2018, *MNRAS*, **474**, 3875
 Balogh M. L., Morris S. L., 2000, *MNRAS*, **318**, 703
 Baugh C. M., et al., 2019, *MNRAS*, **483**, 4922
 Bera A., Kanekar N., Chengalur J. N., Bagla J. S., 2019, *ApJ*, **882**, L7
 Brown T., Catinella B., Cortese L., Kilborn V., Haynes M. P., Giovanelli R., 2015, *MNRAS*, **452**, 2479
 Brown T., et al., 2017, *MNRAS*, **466**, 1275
 Bryan G. L., Norman M. L., 1998, *ApJ*, **495**, 80
 Catinella B., et al., 2018, *MNRAS*, **476**, 875
 Chauhan G., Lagos C. d. P., Stevens A. R. H., Obreschkow D., Power C., Meyer M., 2020, *MNRAS*, **498**, 44
 Chauhan G., Lagos C. d. P., Stevens A. R. H., Bravo M., Rhee J., Power C., Obreschkow D., Meyer M., 2021, *MNRAS*, **506**, 4893
 Chemin L., Carignan C., Foster T., 2009, *ApJ*, **705**, 1395
 Chen Q., et al., 2021, *MNRAS*, **508**, 2758
 Chengalur J. N., Braun R., Wieringa M., 2001, *A&A*, **372**, 768
 Chowdhury A., Kanekar N., Chengalur J. N., Sethi S., Dwarakanath K. S., 2020, *Nature*, **586**, 369

- Chung A., van Gorkom J. H., Kenney J. D. P., Crowl H., Vollmer B., 2009, *AJ*, **138**, 1741
- Cortese L., Catinella B., Boissier S., Boselli A., Heinis S., 2011, *MNRAS*, **415**, 1797
- Cortese L., Catinella B., Smith R., 2021, *Publ. Astron. Soc. Australia*, **38**, e035
- Crain R. A., et al., 2017, *MNRAS*, **464**, 4204
- Davé R., Rafieferantsoa M. H., Thompson R. J., Hopkins P. F., 2017, *MNRAS*, **467**, 115
- Davé R., Crain R. A., Stevens A. R. H., Narayanan D., Saintonge A., Catinella B., Cortese L., 2020, *MNRAS*, **497**, 146
- Delhaize J., Meyer M. J., Staveley-Smith L., Boyle B. J., 2013, *MNRAS*, **433**, 1398
- Diemer B., et al., 2018, *ApJS*, **238**, 33
- Driver S. P., et al., 2011, *MNRAS*, **413**, 971
- Driver S. P., et al., 2022a, *MNRAS*, **513**, 439
- Driver S. P., et al., 2022b, *MNRAS*, **515**, 2138
- Eilers A.-C., Hogg D. W., Rix H.-W., Ness M. K., 2019, *ApJ*, **871**, 120
- Fabello S., Catinella B., Giovanelli R., Kauffmann G., Haynes M. P., Heckman T. M., Schiminovich D., 2011, *MNRAS*, **411**, 993
- Fabello S., Kauffmann G., Catinella B., Li C., Giovanelli R., Haynes M. P., 2012, *MNRAS*, **427**, 2841
- Giovanelli R., et al., 2005, *AJ*, **130**, 2598
- Gnedin N. Y., Draine B. T., 2014, *ApJ*, **795**, 37
- Gunn J. E., Gott J. Richard I., 1972, *ApJ*, **176**, 1
- Guo H., Jones M. G., Haynes M. P., Fu J., 2020, *ApJ*, **894**, 92
- Haynes M. P., Giovanelli R., Chincarini G. L., 1984, *ARA&A*, **22**, 445
- Haynes M. P., et al., 2018, *ApJ*, **861**, 49
- Hotan A. W., et al., 2021, *Publ. Astron. Soc. Australia*, **38**, e009
- Hu W., et al., 2019, *MNRAS*, **489**, 1619
- Hu W., Catinella B., Cortese L., Staveley-Smith L., Lagos C. d. P., Chauhan G., Oosterloo T., Chen X., 2020, *MNRAS*, **493**, 1587
- Jarvis M., et al., 2016, in *MeerKAT Science: On the Pathway to the SKA*. p. 6 ([arXiv:1709.01901](https://arxiv.org/abs/1709.01901)), doi:10.22323/1.277.0006
- Johnston S., et al., 2007, *Publ. Astron. Soc. Australia*, **24**, 174
- Johnston S., et al., 2008, *Experimental Astronomy*, **22**, 151
- Jonas J., MeerKAT Team 2016, in *MeerKAT Science: On the Pathway to the SKA*. p. 1, doi:10.22323/1.277.0001
- Jones M. G., Haynes M. P., Giovanelli R., Papastergis E., 2016, *MNRAS*, **455**, 1574
- Kafle P. R., et al., 2016, *MNRAS*, **463**, 4194
- Kafle P. R., Sharma S., Lewis G. F., Robotham A. S. G., Driver S. P., 2018, *MNRAS*, **475**, 4043
- Kalberla P. M. W., Kerp J., 2009, *ARA&A*, **47**, 27
- Kashibadze O. G., Karachentsev I. D., Karachentseva V. E., 2020, *A&A*, **635**, A135
- Kilborn V. A., Forbes D. A., Barnes D. G., Koribalski B. S., Brough S., Kern K., 2009, *MNRAS*, **400**, 1962
- Lagos C. D. P., Lacey C. G., Baugh C. M., Bower R. G., Benson A. J., 2011, *MNRAS*, **416**, 1566
- Lagos C. d. P., et al., 2015, *MNRAS*, **452**, 3815
- Lagos C. d. P., Tobar R. J., Robotham A. S. G., Obreschkow D., Mitchell P. D., Power C., Elahi P. J., 2018, *MNRAS*, **481**, 3573
- Lah P., et al., 2007, *MNRAS*, **376**, 1357
- Li X., Li C., Mo H. J., Xiao T., Wang J., 2022, *ApJ*, **941**, 48
- Lim S. H., Mo H. J., Lu Y., Wang H., Yang X., 2017, *MNRAS*, **470**, 2982
- Liske J., et al., 2015, *MNRAS*, **452**, 2087
- Lu Y., Mo H. J., Lu Z., Katz N., Weinberg M. D., 2014, *MNRAS*, **443**, 1252
- Maddox N., et al., 2021, *A&A*, **646**, A35
- Merson A. I., et al., 2013, *MNRAS*, **429**, 556
- Meyer M., 2009, in *Panoramic Radio Astronomy: Wide-field 1-2 GHz Research on Galaxy Evolution*. p. 15 ([arXiv:0912.2167](https://arxiv.org/abs/0912.2167)), doi:10.22323/1.089.0015
- Meyer M. J., et al., 2004, *MNRAS*, **350**, 1195
- Meyer S. A., Meyer M., Obreschkow D., Staveley-Smith L., 2016, *MNRAS*, **455**, 3136
- Meyer M., Robotham A., Obreschkow D., Westmeier T., Duffy A. R., Staveley-Smith L., 2017, *Publ. Astron. Soc. Australia*, **34**, 52
- Moore B., Katz N., Lake G., Dressler A., Oemler A., 1996, *Nature*, **379**, 613
- Nelson D., et al., 2018, *MNRAS*, **475**, 624
- Obreschkow D., Croton D., De Lucia G., Khochfar S., Rawlings S., 2009, *ApJ*, **698**, 1467
- Obuljen A., Alonso D., Villaescusa-Navarro F., Yoon I., Jones M., 2019, *MNRAS*, **486**, 5124
- Piffl T., et al., 2014, *A&A*, **562**, A91
- Pillepich A., et al., 2018, *MNRAS*, **475**, 648
- Popping G., Somerville R. S., Trager S. C., 2014, *MNRAS*, **442**, 2398
- Rhee J., Zwaan M. A., Briggs F. H., Chengalur J. N., Lah P., Oosterloo T., van der Hulst T., 2013, *MNRAS*, **435**, 2693
- Rhee J., Lah P., Chengalur J. N., Briggs F. H., Colless M., 2016, *MNRAS*, **460**, 2675
- Rhee J., Lah P., Briggs F. H., Chengalur J. N., Colless M., Willner S. P., Ashby M. L. N., Le Fèvre O., 2018, *MNRAS*, **473**, 1879
- Rhee J., et al., 2023, *MNRAS*, **518**, 4646
- Robotham A. S. G., et al., 2011, *MNRAS*, **416**, 2640
- Roychowdhury S., et al., 2022, *ApJ*, **927**, 20
- Solanes J. M., Manrique A., García-Gómez C., González-Casado G., Giovanelli R., Haynes M. P., 2001, *ApJ*, **548**, 97
- Spinelli M., Zoldan A., De Lucia G., Xie L., Viel M., 2020, *MNRAS*, **493**, 5434
- Stevens A. R. H., et al., 2019, *MNRAS*, **483**, 5334
- Strauss M. A., et al., 2002, *AJ*, **124**, 1810
- Villaescusa-Navarro F., et al., 2018, *ApJ*, **866**, 135
- Yang X., Mo H. J., van den Bosch F. C., Jing Y. P., 2005, *MNRAS*, **356**, 1293
- York D. G., et al., 2000, *AJ*, **120**, 1579
- Zwaan M. A., 2000, PhD thesis, University of Groningen, Netherlands

APPENDIX A: INDIVIDUAL DETECTIONS

We present here the results of the 37 direct detected groups from our study. In Table 2, we provide the properties of all these direct detections, and in Fig. A1 we show the group spectra of all the direct detections.

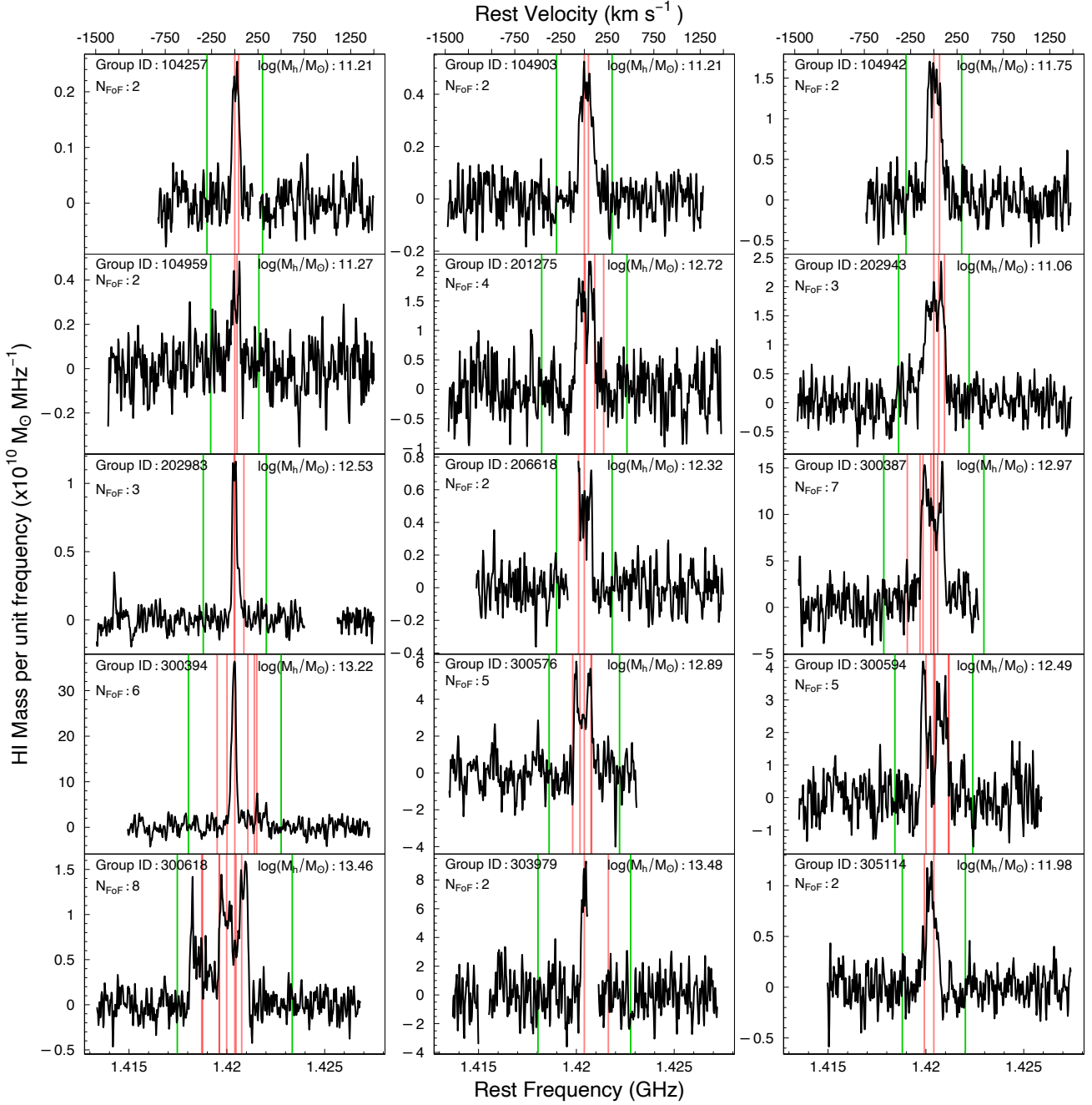


Figure A1. Spectra of all the 37 groups which have detections based on a SNR cut of 3. All the spectra have been shifted to the rest frame. The GAMA Group ID, number of group members and halo mass of the group is shown in each panel. In red lines, the position of various group members are shown. The vertical green line shows the group velocity range.

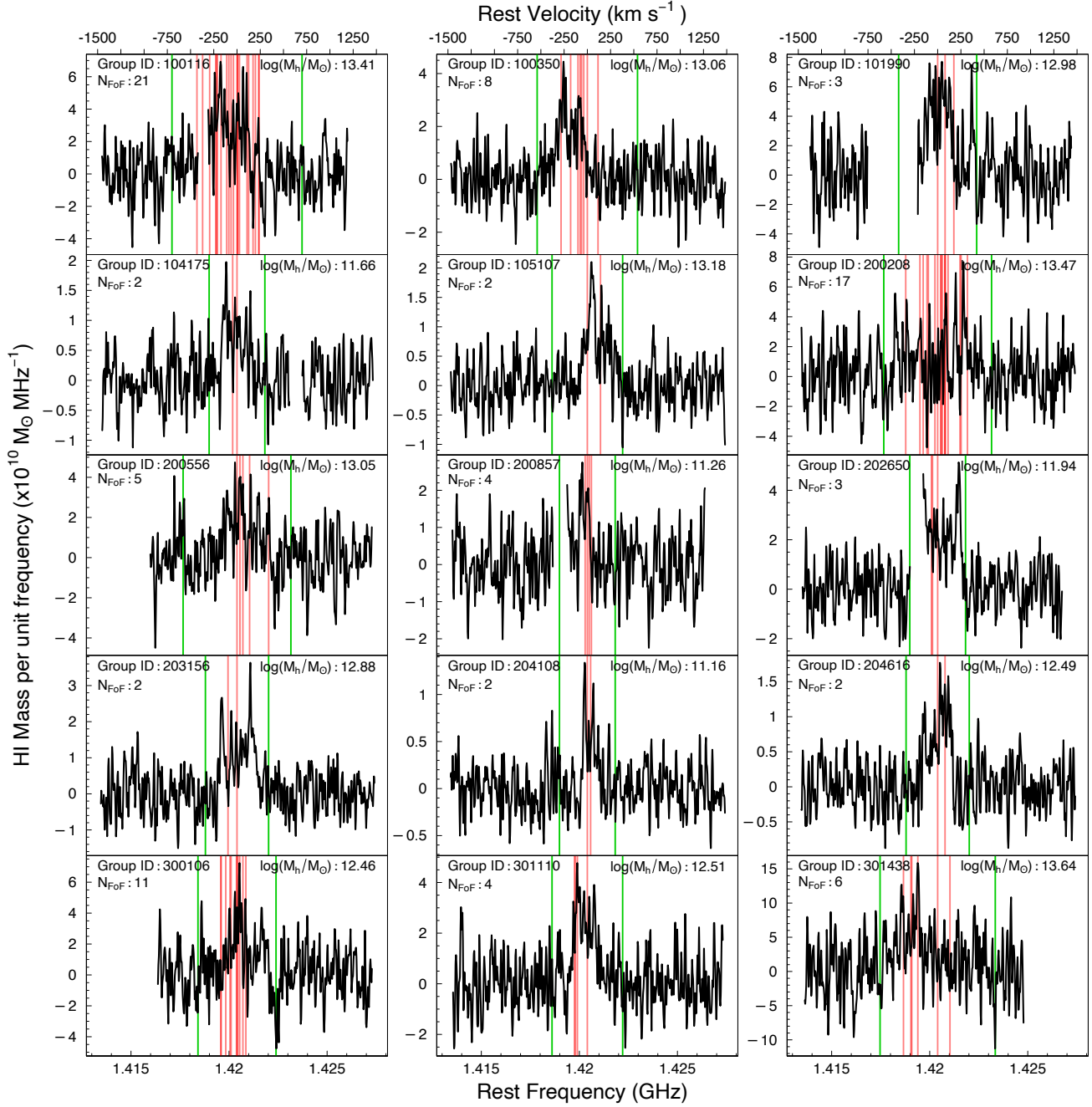


Figure A1. Continued

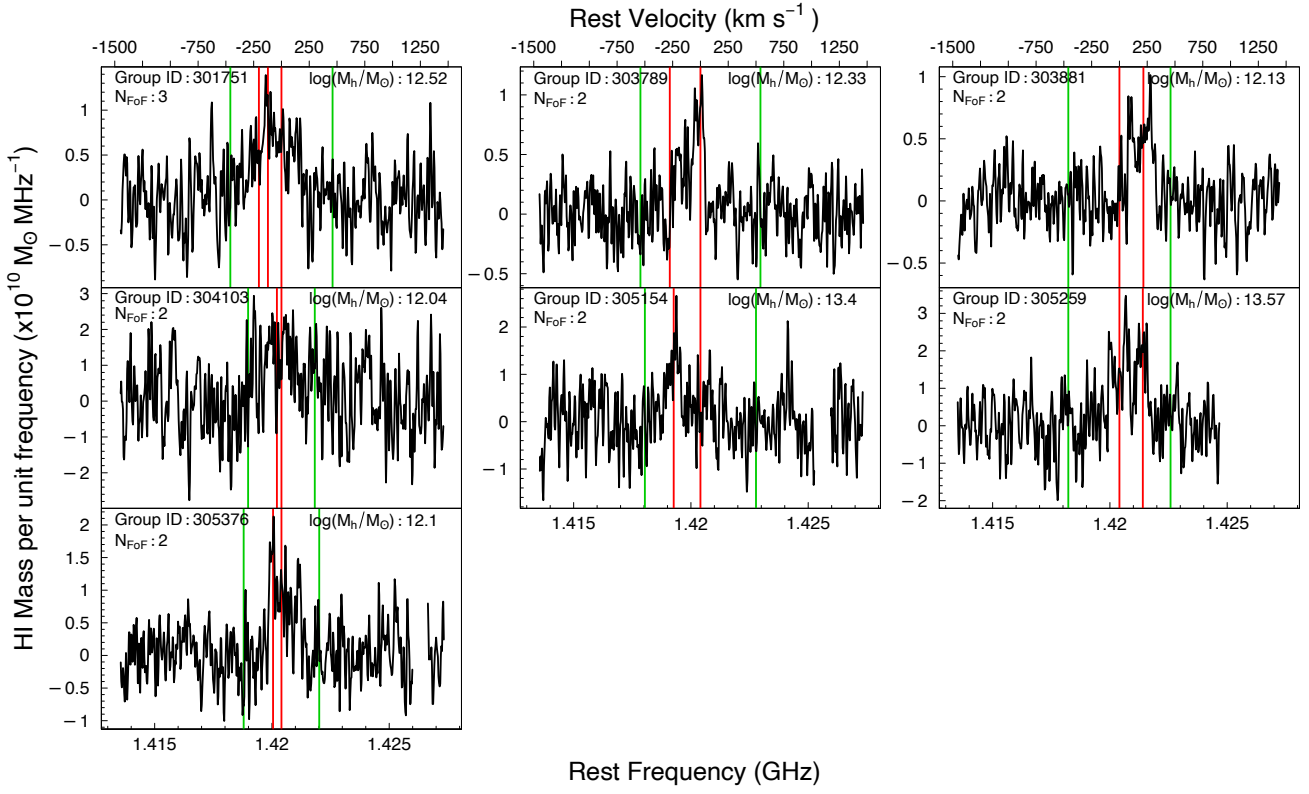


Figure A1. Continued

Group ID	Nfof	$\log_{10}(\text{Halo Mass}/M_{\odot})$	$\log_{10}(\text{H I Mass}/M_{\odot})$
104257	2	11.21 ± 1	9 ± 0.04
104903	2	11.21 ± 1	9.52 ± 0.03
104942	2	11.75 ± 1	10.1 ± 0.02
104959	2	11.27 ± 1	9.39 ± 0.06
201275	4	12.72 ± 0.49	10.16 ± 0.03
202943	3	11.06 ± 0.68	10.36 ± 0.01
202983	3	12.53 ± 0.68	9.59 ± 0.02
206618*	2	12.32 ± 1	9.54 ± 0.03
300387	7	12.97 ± 0.28	11.24 ± 0.01
300394	6	13.22 ± 0.33	11.12 ± 0.01
300576	5	12.89 ± 0.4	10.55 ± 0.03
300594	5	12.49 ± 0.4	10.49 ± 0.03
300618	8	13.46 ± 0.24	10.34 ± 0.02
303979*	2	13.48 ± 1	10.35 ± 0.08
305114	2	11.98 ± 1	9.73 ± 0.03
100116	21	13.41 ± 0.09	10.82 ± 0.03
100350	8	13.06 ± 0.24	10.56 ± 0.03
101990*	3	12.98 ± 0.68	10.93 ± 0.02
104175	2	11.66 ± 1	10.1 ± 0.04
105107	2	13.18 ± 1	10.18 ± 0.02
200208	17	13.47 ± 0.12	10.71 ± 0.04
200556	5	13.05 ± 0.4	10.5 ± 0.06
200857*	4	11.26 ± 0.49	10.09 ± 0.08
202650*	3	11.94 ± 0.68	10.67 ± 0.03
203156	2	12.88 ± 1	10.4 ± 0.03
204108	2	11.16 ± 1	9.65 ± 0.05
204616	2	12.49 ± 1	10.06 ± 0.03
300106	11	12.46 ± 0.17	10.62 ± 0.05
301110	4	12.51 ± 0.49	10.59 ± 0.03
301438	6	13.64 ± 0.33	11.16 ± 0.05
301751	3	12.52 ± 0.68	10.21 ± 0.03
303789	2	12.33 ± 1	9.91 ± 0.03
303881	2	12.13 ± 1	9.82 ± 0.03
304103	2	12.04 ± 1	10.45 ± 0.04
305154	2	13.4 ± 1	10.09 ± 0.06
305259	2	13.57 ± 1	10.48 ± 0.03
305376	2	12.1 ± 1	10.12 ± 0.06

Table A1. Properties of the direct detections. Column 1 - GAMA Group ID, 2 - Number of group members, 3 - Halo Mass the group in log units, 4 - H I mass of the group in log units. The Group IDs which have an asterisk (*) are those that have incomplete spectra due to RFI. The H I masses of these groups should be taken as lower limit.